JOURNAL OF PROPULSION AND POWER
Vol. 26, No. 5, September–October 2010

Thrust Augmentation of Solid Rocket Motors Using Beamed Microwave Energy

Barry Cornella* and Andrew Ketsdever†
University of Colorado at Colorado Springs, Colorado Springs, Colorado 80933
and
Natalia E. Gimelshein‡ and Sergey F. Gimelshein§
ERC, Inc., Edwards Air Force Base, California 93524

DOI: 10.2514/1.48935

A method for augmenting the thrust of a solid rocket motor by coupling beamed microwave energy to alumina particles in the diverging section of a nozzle is analyzed. Coupling of microwave radiation with micron-sized alumina particles increases the particle temperature. The main mechanism of thrust increase is expected to be gas–particle collisions that transfer the increased energy of particles to kinetic energy of the expanding gas. A dynamic power-generation and beaming scheme has been designed to produce 1.0 GW of power at a launch vehicle throughout the first 50 km of its ascent trajectory. Microwave coupling to alumina particles has been investigated experimentally. A two-phase, two-way coupled numerical model has also been developed to assess the increase in propulsive performance. The developed numerical capability has been used to calculate nozzle flowfields for two different solid rocket motors with and without the addition of beamed microwave radiation. High gas density and fast collisional relaxation result in the efficient transfer of microwave energy to the kinetic energy of the flow. The total thrust in both cases was found to increase by approximately 0.5% for a 100 MW/m^2 microwave beam and by 6% for a 1 GW/m^2 beam.

Nomenclature

C_p	=	heat capacity, J/kg K
c	=	speed of light, m/s
d	=	diameter, m
f	=	microwave radiation frequency, Hz
I	=	intensity of microwave radiation, W/m^2
n	=	number density, m^{-3}
Pr	=	Prandtl number
p	=	pressure, Pa
Q	=	heat flux, W/m^2
Re	=	Reynolds number of particles
T	=	temperature, K
T_{p_j}	=	jth particle temperature, K
t	=	time, s
$\tan\delta$	=	energy-loss factor
u_{g_i}	=	ith component of gas velocity, m/s
u_{p_i}	=	ith component of particle velocity, m/s
V, u	=	velocity, m/s
Δt	=	time step for particle tracking, s
ϵ_m	=	product of the permittivity of free space and the real part of the dielectric permittivity
λ	=	gas thermal conductivity, W/m K
ν	=	gas viscosity, Pa s
ρ	=	density, kg/m^3
τ_{ij}	=	shear stress tensor, Pa

Subscripts

g	=	gas
p, part	=	particle

I. Introduction

BEAMED energy propulsion is a technique that uses electromagnetic radiation from a remote source to increase the energy of a propellant. The electromagnetic radiation, in general, can originate from any source, although the most recent concepts feature either high-power laser beams or microwaves. One significant advantage of beamed energy propulsion is that it requires little to no additional mass to be carried onboard the vehicle. Beamed energy propulsion can also overcome the inherent limitations on specific impulse imposed by chemical energy production mechanisms. The idea of beamed energy propulsion was first put forward by Konstantin Tsiolkovsky [1] in 1924 and then later expanded on by Shad and Moriarty [2], who first proposed the concept of launching objects specifically with beamed microwave (MW) energy from a ground-based source. Since the work of Shad and Moriarty, a great deal of research has been done leading to a wide variety of beamed MW propulsion concepts as well as significant advances in MW generation [3–7].

Launch concepts based on beamed energy propulsion generally fall into one of three categories: 1) direct energy coupling to the propellant, 2) energy addition to a heat exchanger, or 3) energy coupling via plasma formation. This analysis will look at directly coupling MW energy to the effluents of a solid rocket motor in the diverging section of the nozzle, as shown in Fig. 1. Through direct energy coupling, this concept involves augmenting the thrust of an existing rocket by first heating liquid alumina particles produced by the thruster, then transferring that energy to the expanding gas via gas–particle collisions. Simply augmenting the thrust of an existing rocket has several distinct advantages. First, since the MW energy radiates from a remote, ground-based source, the mass increase on the vehicle itself is minimal. Second, only the diverging section of the nozzle would need altering to handle higher-temperature operation, since the power addition only occurs in this section. Finally, the enhanced performance provided by this beamed propulsion concept

Presented as Paper 2009-4962 at the 45th Joint Propulsion Conference, Denver, CO, 4–7 August 2009; received 14 January 2010; revision received 22 April 2010; accepted for publication 4 May 2010.

*Graduate Research Assistant, Mechanical and Aerospace Engineering. Student Member AIAA.
†Assistant Professor, Mechanical and Aerospace Engineering. Associate Fellow AIAA.
‡Consultant. Senior Member AIAA.
§Senior Research Engineer. Senior Member AIAA.

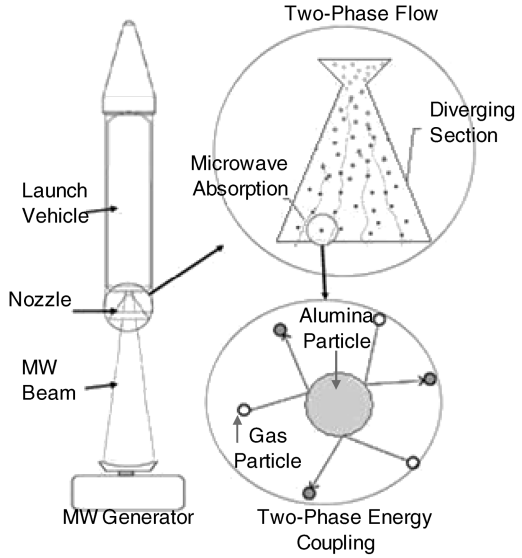

Fig. 1 MW thrust augmentation through direct coupling to alumina particles.

can lead to the reduction in the complexity of launch vehicle staging and possibly single-stage-to-orbit operation.

Thrust augmentation using beamed energy does have several technical challenges. First, MW coupling to supersonic two-phase flow needs to be investigated. Next, MW heating in undesired locations within the launch vehicle could pose thermal and structural issues that will need to be addressed. For example, increased thermal loading would require modifications to the launch vehicle that could add additional complexity and mass. Finally, because large power densities are required, the infrastructure cost of a high-power ground-based facility will be quite high.

The second of the aforementioned categories has been studied primarily by Parkin [3], who developed a concept for a microwave thermal thruster that uses beamed MW power at a heat exchanger attached to the launch vehicle. The heat exchanger absorbs the energy and transfers it to a hydrogen propellant flowing through an array of small channels. Parkin et al. [4] indicate that a hydrogen propellant is capable of producing 54 kN of thrust with a specific impulse of over 1000 s. It has been estimated that a 1 t vehicle can carry 100 kg of payload to an 1100 km circular orbit using 275 MW of beamed energy [5]. This system offers the benefit of higher exhaust velocities over traditional chemical rockets and thus higher specific impulse.

Researchers at the University of Tokyo have investigated a concept using beamed MW energy to produce plasma near the focal point of the directed beam [6,7]. The formed plasma then absorbs the remaining MW pulse to increase the enthalpy of the propellant. The vehicle uses repetitive pulses to induce plasma in either a stored propellant or the surrounding air to propel the vehicle. Both systems proposed by the researchers at the University of Tokyo and by Parkin [3] use beamed MW power as the sole source of propulsive force. The concept in this paper, in which MW augmentation merely enhances the vehicle performance, can be viewed as a potential short-term alternative to these aforementioned concepts. This could significantly reduce the risk of attempting to launch an initial beamed MW vehicle while providing a technology demonstration for the concepts derived by other authors. Other advantages to the proposed concept include no mass increase due to a heat exchanger and no energy losses due to plasma formation.

The purpose of this study is to provide a numerical basis for a concept that increases the thrust of a solid rocket motor using beamed MW energy. The performance of a notional Castor 120^{TM} is studied in both unaugmented (baseline) and augmented scenarios. Although the Castor 120 solid rocket motor is by no means optimized for a thrust-augmentation application, it provides a baseline design with well-quantified performance characteristics. The performance of an Orion 50S XL^{TM} (first stage of a Pegasus launch vehicle) was also evaluated. The unaugmented mass and performance characteristics of the Castor 120 and Orion 50S XL motors are shown in Table 1 [8,9]. In the augmented case, the motors are augmented for the first 50 km of its vertical ascent. An altitude of 50 km was chosen based on potential beam propagation issues through the atmosphere beyond this altitude. In general, the augmentation (MW energy addition) was assumed to bring the alumina particles in the nozzle to their boiling point of 3250 K. The critical analysis presented in this paper is threefold. First, a power-generation scheme is outlined to provide the necessary electromagnetic energy to the vehicle at 50 km. Second, an experimental study is presented involving the MW coupling efficiency of solid aluminum oxide (alumina) particles at room temperature with a 2.45 GHz MW power source. Third, a computational fluid dynamics (CFD) analysis is presented, evaluating the two-phase flow characteristics with energy coupling associated with the system. Included in this analysis are the performance characteristics of both the Castor 120 and the Orion 50S XL with energy addition.

II. Power Generation

The power-generation system proposed in this study was designed to produce a nominal 1.0 GW at the vehicle throughout the first 50 km of its ascent trajectory. At this altitude, the launch vehicle has passed through the densest part of the atmosphere. The antenna array design presented here is comparable to other power-generation schemes developed in previous papers [4,10,11] with a few modifications in both array structure and operation. Designing the ground-based MW transmitter requires the consideration of several factors. Initial parameters include the source of MW power, the optimal transmitted frequency, and physical structure. Operational considerations as well as the required size and power parameters are then determined.

A. Initial Parameters

One stipulation set for this system is that the technology is available today as commercial-off-shelf components. This led to the selection of gyrotrons as the electromagnetic power source. Currently, gyrotrons are being used to produce waves in the 100 to 280 GHz frequency range at the megajoule level. Commercially available gyrotrons are capable of producing 140 GHz at 1 MW average power in a continuous wave operation [12]. A frequency of 140 GHz was chosen based on atmospheric breakdown and attenuation effects. Figure 2 shows the combined free-space and atmospheric attenuation losses for a typical gyrotron frequency range. The antenna structure consists of a closely packed array of parabolic antenna elements for high beam directivity. Each element is phase-controlled so that the array beam can produce maximum power output as well as be electronically steered for vehicle tracking.

B. Operation/Power Budget

Unlike previous ground system models, the purpose of the power-generation system is to provide power to the vehicle at a relatively constant intensity with roughly the same spot area throughout the flight. For this reason, dynamic system operation is required. The ground facility was designed to deliver 1.0 GW to the vehicle at 50 km into its ascent trajectory. To avoid atmospheric breakdown

Table 1 Castor 120 and Orion 50S XL characteristics

Characteristic	Castor 120	Orion 50S XL
Burn time	79 s	68 s
Average vacuum thrust	1,687, 655 N	721,000 N
Dry mass	4071.5 kg	1386 kg
Propellant mass	49,005 kg	15,032 kg
Expansion ratio	17.3	34.3
Exit diameter	1.52 m	0.712 m
Vacuum specific impulse	280.2 s	293 s
Vacuum exit velocity	2750m/s	2870 m/s
Jet power	2.3 GW	1.2 GW

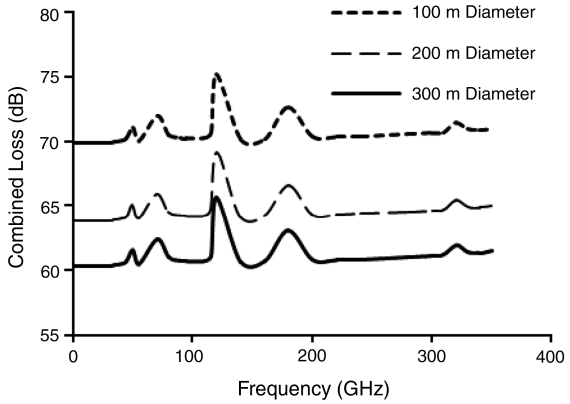

Fig. 2 Combined losses from atmospheric attenuation and free-space loss for various-sized antennas.

with the 140 GHz beam, a half-power spot diameter (defined as the diameter of the spot area, which contains half the total power of a Gaussian beam) was chosen to be 1.5 m at the vehicle. From diffraction-limited optics with a maximum angle off zenith of 45°, the effective diameter for the system was determined to be 207 m for this spot diameter.

Because of the large diameter of the array and the relatively small beam wavelength, the near-field region of the antenna extends well beyond the 50 km operating range for the system. Therefore, a nontraditional power budget method was employed to determine the system's power parameters. For this case, a method first introduced by Brown [13] was used in which power transmission is represented through a series of efficiencies. The total free-space transmission efficiency is a function of subefficiencies associated with the conversion of DC power to MW power, the antenna illumination, the path loss through transmission, etc. The total transmission efficiency at 50 km is approximately 32% (for a complete analysis of each efficiency, see [14]). The system therefore requires 3.13 GW of input power to produce 1.0 GW at the launch vehicle at 50 km. A total of 1.77 GW is produced at the surface of the array, corresponding to 1770 gyrotrons operating at a peak power of 1 MW each.

One way to vary the power and spot diameter of the array throughout the launch is to activate a fraction of the antenna elements at the beginning of the launch and gradually increasing the number of powered elements as the launch progresses. In this case, elements are grouped into ring sections, which in turn are progressively powered on during the launch. Figure 3 shows a snapshot in time (corresponding to a vehicle altitude of 27 km) in which six ring sections are illuminated. Note that the innermost ring section contains smaller elements than the rest of the array. To produce sufficient power (from fewer elements) at the start of the launch, more gyrotrons need to be concentrated at the center. Thus, more antenna elements must be located in the center to avoid overloading any particular element with too many gyrotrons. Smaller elements must be employed in the center to resolve the space issue created by loading more elements in the center of the array. Overall, there are 520 antenna elements with a diameter of 9 m and 145 elements with a diameter of 2.25 m. Figure 4 shows the number of gyrotrons powered as a function of vehicle altitude. The array illuminates in 12 discrete steps, corresponding to the 12 ring sections contained in the array. Table 2 shows a summary of the ground system's parameters.

III. MW Coupling to Alumina Particles

The process of coupling MW energy to alumina particles in the solid rocket motors exhaust is important to assess the potential of this concept study. The thrust-augmentation process can be achieved in one of two ways: 1) heating alumina droplets with MW energy and transferring that energy to the expanding gas through collisions or 2) vaporizing the alumina droplets through the MW energy and adding molecular species to the flow. Because of the relatively high latent heat of vaporization of alumina, vaporization is not expected to

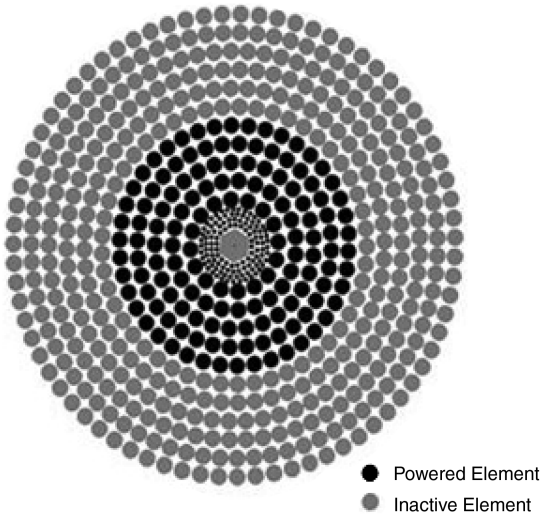

Fig. 3 Operational control of phased array at 27 km.

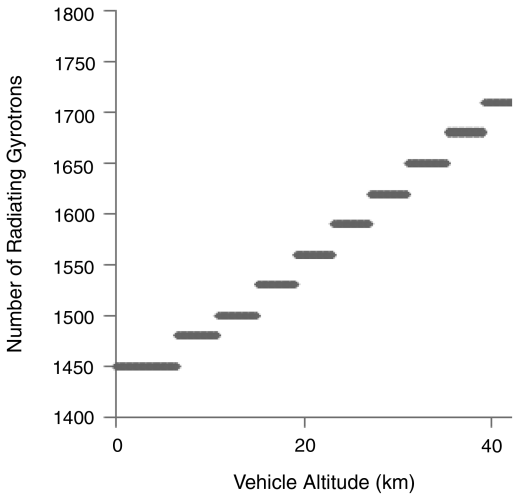

Fig. 4 Number of powered gyrotrons vs vehicle ascent altitude.

contribute to the overall augmentation process. Therefore, thrust augmentation will occur in a two-step process. First, the alumina particles will be heated in the diverging section of the nozzle (through MW addition) from their nominal combustion chamber temperature of approximately 2500 K to their boiling temperature of approximately 3250 K. Constant MW energy addition will allow the particles to maintain a temperature of 3250 K throughout the nozzle. The particles then are used as a heat exchanger with the surrounding gas. Through gas–particle collisions, the gas enthalpy is increased. As the gas expands through the nozzle, it converts the imparted thermal energy to kinetic energy, thus increasing the thrust. For the purposes of this study, an experiment was conducted to investigate the coupling efficiency between alumina particles and MW energy.

Table 2 Antenna design summary

Specification	Value
Input power	3.13 GW
Power produced by array	1.77 GW
Power at 50 km	1.0 GW
Effective diameter	207 m
Number of antenna elements at 9 m	520
Number of antenna elements at 2.25 m	145
Number of gyrotrons (at 1 MW)	1770

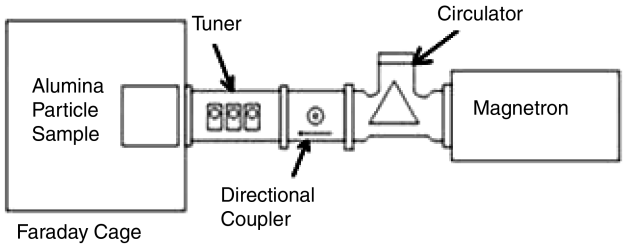

Fig. 5 Experimental setup.

A. Experimental Setup

The purpose of this experiment was to generate a coupling efficiency for solid alumina particles being irradiated by MW energy. To estimate the coupling efficiency, a comparison of the power of a 2.45 GHz system to a standard plate heater at the same steady-state temperature was performed. A sample of alumina powder with an average particle size of 10 μm was radiated in a 0.23 m^3 Faraday cage with a 2.45 GHz magnetron. The temperature of the particles was monitored using an infrared pyrometer from outside the Faraday cage. A diagram of the experimental setup is shown in Fig. 5. First, a sample of alumina particles was irradiated with the magnetron until they reached a steady-state temperature. Temperature measurements were then taken a rate of 1 Hz for the period of 1 h. The MW source forward and reflected power were measured. The difference between the forward and total reflected microwave power was assumed to be the power absorbed by the alumina powder. A second experiment was conducted to confirm the findings from the forward and reflected power from the magnetron. Alumina particles were heated using a resistive heater to the same steady-state temperature by placing the alumina powder directly on the resistively heated surface. Therefore, in this experiment, heating of the alumina powder occurred only through thermal conduction. The heater voltage was varied using a variable transformer and the power output from the heater was measured. The efficiency of the resistive heater was assumed to be close to 100%. The temperature of the resistive heater surface was measured using a standard thermocouple, and the temperature of the alumina powder was monitored using the same pyrometer setup as the MW test at the same emissivity. Measurements were taken when the resistive heating surface temperature was the same as the alumina powder temperature. To obtain the coupling coefficient for the alumina particles, the ratio of power from the heater to the power from the MW system (at the same steady-state temperature) was calculated. Both methods gave the same results for the alumina powder-MW coupling coefficient to within 5%.

B. Experimental Results

During the MW test, the alumina powder reached a steady-state temperature of approximately 816 K, as shown in Fig. 6. The downstream (forward) MW power level reaching the alumna powder during this test remained relatively constant at 1.811 kW. Within 10 s of full MW power, the particles exhibited rapid energy absorption as indicated in Fig. 6. The sample was then cooled and reheated using the resistive heater to the same steady-state temperature with an input power of 1.033 kW. Assuming that the losses by both the resistive heater and the MW systems are the same, the efficiency of MW absorption by the alumina particles was found to be 57.1%, taking the ratio of the power levels required by the two heating systems.

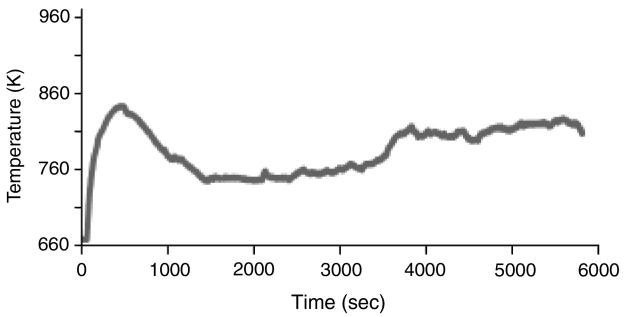

Fig. 6 Pyrometer temperature data for MW irradiation of alumina particles.

In developing the coupling efficiency, several assumptions were made. First, the losses due convective cooling and conduction through the Faraday cage were assumed to be the same for both the MW and resistive heater configurations and were therefore neglected in the calculations. The emissivity of the sample was also assumed to be constant through the heating process. The instrumentation in this experiment induced a certain amount of error in the power calculations. The MW power meter has a resolution of 4 W and an accuracy error of 0.01%, yielding a percent error of 0.1%. The power measurements for the resistive heater have errors of approximately 4%. The total coupling efficiency error due to instrumentation was approximately 2.2%.

C. Extrapolation of Results to Solid Rocket Motors

The aluminum oxide (alumina, Al_2O_3) produced in a typical solid rocket motor is formed as a liquid in the combustion chamber. These liquid droplets cool rapidly and solidify through the expansion region of the nozzle but can remain above 1500 K for a typical motor. Generally, the cooling and solidification of liquid droplets through a given nozzle is driven by the particle size. The liquid droplets range in size from 0.1 to 20 μm with a mean size for the Pegasus first stage of around 10 μm (see, for example, [15]). The liquid droplets solidify into γ alumina, which may eventually transform into α alumina, depending on the subsequent cooling process. Several studies [16–18] indicate that alumina absorption of MW radiation increases with increasing temperature, due to an increase in the polarizability of the material caused by volumetric expansion. The experimental results presented in the previous section indicate that a significant fraction of the incident MW energy was absorbed by solid alumina initially at room temperature within 10 s of exposure to the MW beam. Therefore, high-temperature liquid alumina has the potential to absorb a significant fraction of an incident MW beam within the residence time of the particles in the diverging section of the nozzle (i.e., on the order of milliseconds). For alumina, MW absorption is assumed to be phase-dependent and not particle-size-dependent. Therefore, the experimental results for 10-μm-diam particles are expected to be valid in terms of energy absorption for the various-diameter particles found in a typical solid rocket motor.

IV. Development of Numerical Model for Two-Phase Flow with Energy Addition

A combined Eulerian–Lagrangian approach with two-way coupling was used to model the impact of the MW radiation on the two-phase flow inside the nozzle of a solid rocket motor. Gas properties were computed using an Eulerian approach based on the solution of the Navier–Stokes equations with appropriate source terms, taking into account the impact of particulates on the gas flow, and can be written as

$$\frac{D\rho}{Dt} + \rho(\nabla \cdot \mathbf{V}) = 0 \tag{1}$$

$$\rho\frac{D\mathbf{V}}{Dt} - \nabla \cdot \mathbf{\Pi}_{ij} = D_i \tag{2}$$

$$\rho\frac{D\mathbf{V}}{Dt} \cdot \mathbf{V} + \nabla p \cdot \mathbf{V} - (\nabla \cdot \tau_{ij}) \cdot \mathbf{V} = Q \tag{3}$$

where

$$D_i = 3\pi d_{\text{part}} n_{\text{part}} \nu (1 + 0.15 \times Re^{.687})(u_{pi} - u_{gi}) \tag{4}$$

and

$$Q = 2\pi d_{\text{part}} n_{\text{part}} \lambda (1 + 0.3\sqrt{Re}) Pr^{\frac{1}{3}} (T_p - T_g) \tag{5}$$

Here, Reynolds and Prandtl numbers are defined as

$$Re = \rho_g d_{\text{part}} |\mathbf{u}_p - \mathbf{u}_g| / \nu \quad \text{and} \quad Pr = \nu C_{p_g} / \lambda \tag{6}$$

The Navier–Stokes equations were solved using the Versatile Advection Code (VAC) [19], modified to include the above particle source terms. Particle properties were determined by Lagrangian tracking of particles through the gas flowfield and statistical averaging of particle properties. Developed in this work, the Lagrangian particle tracker, combined with the Eulerian gas phase module (modified VAC) into a two-phase flow solver VAC-2P, was used to obtain two-phase flow solutions through two successive steps. First, a steady-state solution of gas flow was computed, with the particle source terms set to zero. Then alumina particles were introduced at the nozzle throat, with their surface temperature and velocities set to the corresponding gas temperature and velocities, and the steady-state two-phase flow solution was computed. For the gas phase, an explicit time integration with a Courant–Friedrichs–Levy value of 0.4 was used, and the Navier–Stokes equations were solved using the TVD–Lax–Friedrichs scheme with a minmod limiter. For the particle phase, a fourth-order Adams–Moulton method was used to integrate particle equations of motion. The force on the particle was calculated as

$$F_i = 3\pi d_{\text{part}} \nu (1 + 0.15 * Re^{.687})(u_{pi} - u_{gi}) \tag{7}$$

where the Reynolds number is based on the individual particle velocity. The particle temperature at the next step was determined as

$$\Delta T = \frac{12\Delta t(1 + 0.3\sqrt{Re}Pr^{1/3})\lambda_f}{C_{p_{\text{part}}} \tilde{\rho}_p d_{\text{part}}^2} (T_g - T_{pj}) + \frac{\Delta t 4\pi f \epsilon_m \tan \delta I}{c C_{p_{\text{part}}} \rho_p} \tag{8}$$

Different time steps were used for the integration of the Navier–Stokes equations and particle tracking, with particle-tracking time step approximately an order of magnitude larger than the Eulerian-stage time step. Particle macroparameters (number density, temperature, and velocity) used in the Eulerian source terms were determined by simple averaging over each cell.

V. Two-Phase Flow Analysis

First, a two-phase flow through a Castor 120 nozzle in the absence of any MW heating was considered. Two CFD solvers were used for modeling of this flow: 1) the VAC-based solver VAC-2P discussed in the previous section and 2) a commercial software package CFD++ [20]. They will be referred to as model 1 and model 2, respectively. Comparison of a new VAC-based two-phase capability with an established CFD solver provides additional confidence in model validation and the basis for further accuracy analysis. The axisymmetric coordinate was used with a second order spatial scheme. A general multiphase capability has been used that provides an Eulerian description of the disperse phase (particulates).

For models 1 and 2, the computational domains were meshed with a 7200 rectangular cell grid, encompassing the diverging part of the nozzle and the plume flow in the vicinity of the nozzle. Our preliminary computations with model 2 have shown that the impact of the combustion chamber and the converging part of the nozzle on the flow in the diverging part of the nozzle and at the nozzle exit is relatively small, and therefore only the diverging part of the nozzle is considered here. For the high-density flow considered in this work, the boundary layer near the nozzle throat is very thin. Therefore, uniform boundary conditions were applied at the nozzle throat, with gas density, velocity, and temperature of 3.54 kg/m^3, 1019 m/s, and 2500 K, respectively. A supersonic outflow boundary condition was used at the nozzle exit plane, and the adiabatic condition was prescribed at the wall. To simplify the analysis, a single effective perfect-gas species and a single alumina particle diameter of 4 μm were considered in the simulations. The particle mass loading of 32% was specified at the nozzle throat, and particle temperature and velocity at the throat were assumed to coincide with the corresponding gas properties.

The gas temperature and particle surface temperature obtained with both flow solvers are presented in Fig. 7. The transient heat conduction inside the particles is not considered, and particles are assumed to have a single material temperature (surface temperature, or simply temperature hereafter). Comparison of the two solutions shows good agreement between their gas temperatures in the first half of the nozzle, whereas there is a visible difference between the solutions in the second half of the nozzle and in the plume. At the nozzle exit, the gas temperature obtained by model 1 is over 100 K higher than model 2. The particle temperature at the exit plane predicted by model 1 is up to 20 K lower than in model 2. The difference between their particle temperatures in the first half of the nozzle can also be noted, with the solution from model 1 being lower. Excellent agreement between their gas-only solutions, obtained in preliminary studies (not shown here), allows the authors to attribute the differences between the two solutions to the differences in the particle-gas heat transfer and drag models used in the two solvers. There is obviously a stronger heat transfer coupling between alumina particles and gas flow in model 1 than in model 2. Nonetheless, the observed differences in the solutions, although noticeable, are significantly smaller than those obtained earlier among other commercial codes [21].

Comparing the gas and particle temperature fields computed with model 1, the gas temperature decreases quickly from 2500 K at the nozzle throat to about 1300 K at the nozzle exit. The maximum temperature along the nozzle exit plane is observed near the nozzle wall, due to the formation of the boundary layer (even though the boundary layer occupies a relatively small part of the nozzle). The rapid gas expansion and corresponding cooling results in a

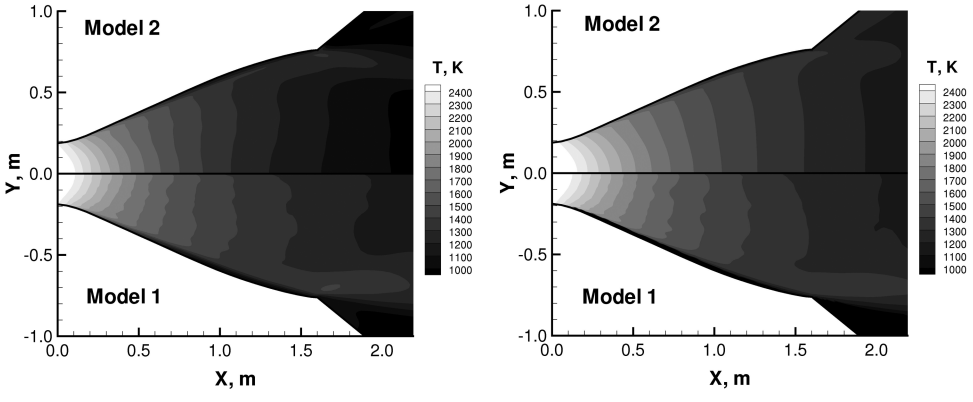

Fig. 7 Castor 120 temperatures (K) for the no-MW-radiation case: a) gas and b) alumina particle.

significant decrease of the particle surface temperature inside the nozzle. For the flow conditions inside the nozzle, the gas density is high enough for the gas-to-particle heat transfer to be dominant and the gas and particle temperatures to be nearly equal. As gas expands and its density decreases, the particle drag force also decreases, and thus the difference between the particle and gas temperatures becomes visible, increasing the temperature difference from a few degrees near the nozzle throat to about 30 K in the plume. In the core flow at the nozzle exit plane, the particle temperature is about 20 K higher than the gas temperature. Near the wall, this difference is smaller and amounts to less than 10 K. The important conclusion from the analysis of the temperature fields is that heat transfer coupling between gas and particles in a Castor 120 motor is high enough for any change in particle temperature, due to MW heating to be immediately transferred to the gas. This implies that even though the gas is not significantly heated when exposed to the MW radiation, alumina particle heating may be a robust mechanism for increasing the gas enthalpy.

The second most important parameter is the gas velocity, since increasing gas velocity at the nozzle exit through the MW heating is the main goal of the MW energy deposition. The gas and particle axial velocity fields obtained with both numerical approaches are shown in Fig. 8a and 8b, respectively. The two solutions are very similar in the first half of the nozzle; however, there are somewhat smaller gas and particle velocities near the nozzle exit and in the plume for the model 1 solution. This is related to the differences in gas–particle heat and momentum transfer models used in the two solvers. It is worth noting that the model 1 solution predicts no particles in the plume for angles larger than the nozzle exit angle (particles are too heavy to be turned at larger angles). Therefore particle velocities are undefined in that region. In model 2, which uses an Eulerian description of particulates, there is some small fraction of particulates at high angles (corresponding to very high velocities of over 2400 m/s), but they are of numerical (and not physical) origin.

Analysis of the model 1 solution shows that the velocity increase is most significant in the first third of the diverging part, where it increases by approximately a factor of 2 to about 2000 m/s. In the last third of the nozzle, the increase is relatively small: only about 100 m/s. The gas exit velocity near the nozzle axis is about 2700 m/s. The position of the boundary layer is clearly seen; at the nozzle exit plane, its thickness is slightly more than 10% of the nozzle exit radius. The alumina particle axial velocity field is qualitatively and quantitatively very similar to that of the gas. At the nozzle exit plane, it is only about 50 m/s lower than the gas velocity, which amounts to 2% of the total velocity magnitude. This indicates that the drag force is very significant inside the nozzle, and the increase in gas velocity due to enthalpy addition to the flow will be accompanied by a similar increase in particle velocity. In terms of the MW–particle interaction, this may result in a considerable reduction of the interaction time for a given nozzle geometry.

VI. Physical Mechanisms of the MW/Two-Phase Fluid Coupling

The immediate effect of the interaction of MW radiation with the two-phase flow inside the diverging part of a solid rocket motor is expected to be an increase of alumina particle temperature. This in turn will result in an increase in gas temperature and then gas and particle velocities. The schematics of such an interaction are shown in Fig. 1. It is clear that the ability of the MW radiation to considerably improve the performance of a thruster through the interaction with the expanding flow greatly depends on flow parameters in the diverging part of the nozzle. The coupling of the radiation with a two-phase flow in a solid rocket motor is mostly determined by the properties of the alumina particles that are expected to dominate the radiation-to-media heat transfer in the absence of significant gas ionization. The macroparameters of alumina particles (such as their temperature, size distribution, and number density) influence the amount of radiation being absorbed by the media. The performance of the thruster impacted by the MW radiation strongly depends on the feedback from the gas, the impact of the walls, and the fact that much of the radiation is expected to be absorbed as the photons travel upstream in the diverging part of the nozzle.

Generally, two important issues impact the thruster performance increase due to the energy deposition from MW radiation to alumina particles inside the nozzle. The first is related to the possibility of MW photons to heat particles fast enough to sufficiently high temperatures. The second is associated with the efficient transfer of internal energy of the particles to the gas with successive conversion of the gas molecule thermal motion to the directional motion along the nozzle axis. The above numerical analysis shows the possibility to effectively transfer heat from the particle surface to the gas inside the diverging part of the nozzle. The first issue is more difficult to estimate, however. The rate of the heating of a particle exposed to MW radiation can be calculated using the second term of Eq. (8) [22].

While the material properties of alumina are reasonably well known, the electric field properties are particular to the MW generator setup. The alumina microwave properties at very high temperatures are also not well known. The authors are not aware of any experimental data in which the MW energy dissipation in alumina would be measured at temperatures in the range from 2300 to 3000 K, although there are a significant number of papers devoted to the low-temperature alumina optical properties (see, for example, [23]). The situation is complicated by the fact that there are several alumina phases present in the exhaust, from liquid alumina (for temperatures higher than the alumina melting temperature of 2350 K) to γ alumina at lower temperatures to α alumina, with partially melted particles also being present in large numbers. Different phases are expected to have different optical properties in the MW range, similar to the properties in the ultraviolet and infrared band known from other experimental studies. Another difficulty is

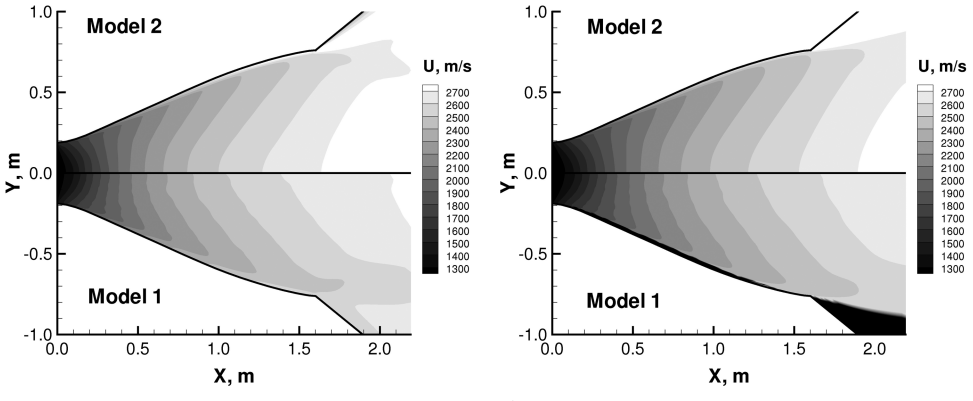

Fig. 8 Castor 120 axial velocity (m/s) for the no-MW-radiation case: a) gas and b) particle.

related to the impurities inherent in alumina particles in the exhaust. Even though the impurities may amount to less than 1% of the total particle mass, they may significantly change (and generally increase) the MW energy dissipation [16].

Experimental studies of 92% pure α alumina have been conducted [18,24], and the dielectric loss factor $\varepsilon' \tan(\delta)$ has been measured for temperatures from about 300 to 2100 K at 6 GHz. It is interesting to note that starting from approximately 600 K, the loss factor increases exponentially, from below 0.01 to more than 1 at 2100 K. Extrapolation of the exponential dependence to the alumina particle temperatures at the nozzle throat gives the loss factor of about 10. Analysis of the alumina optical properties of different purities for temperatures up to about 1600 K, based on existing experimental data, was conducted in [16]. The relative dielectric constant ε' is a weak function of temperature, increasing for 99% pure alumina from 9.5 at room temperature to approximately 11 at 1600 K. The loss tangent strongly increases with temperature, however. At a temperature of 1600 K it amounts to about 0.01 for 97% pure alumina and 0.004 for 99% pure alumina, which results in loss factors of about 0.1 and 0.04, respectively. Assuming an exponential dependence of the loss factor on temperature and extrapolating it to higher temperatures, one may expect to have a loss factor on the order of 10 for the flow conditions near the nozzle throat. The value of 10 has therefore been used in this work. The effective lifetime of particles in the diverging part of the nozzle may be estimated at approximately 1 ms. For a 10 GHz beam and an electric field intensity of 1 GW/m^2, the average increase in particle temperature well in excess of 2,000 K is expected from Eq. (8). This is a clear indication that the alumina particles may be heated quickly inside the nozzle and maintained at their boiling temperature of 3250 K. No significant amount of alumina vaporization is expected, due to an extremely high heat of vaporization of 1.9 MJ/mol.

VII. MW/Two-Phase Nozzle Flow Coupling

The high thermal and velocity coupling between the gas and particulate phases in a Castor 120 nozzle flow shown in the previous section enables an efficient transfer of radiation energy from an incoming MW beam to thermal and then kinetic gas energy. The results presented below are obtained with model 1 via a one-way coupling of a MW beam entering the nozzle and a two-phase flow with parameters and models used in the previous section. The MW beam is assumed to enter the nozzle from the nozzle exit plane and then propagate upstream to the nozzle throat. Two constant MW intensities are considered here, 100 MW/m^2 and 1 GW/m^2.

The particle and gas temperature fields are presented in Fig. 9 for three cases: 1) no MW beam, 2) 100 MW/m^2, and 3) 1 GW/m^2. Comparing the first two cases, it is clear that the interaction between the MW radiation and alumina particles causes a noticeable increase in particle temperatures (Fig. 9a). The difference between particle temperatures in these two cases increases as the flow moves through the nozzle, reaching its maximum of about 150 K near the nozzle exit plane. The increase is practically the same in the core flow and near the nozzle surface. The higher MW intensity of 1 GW/m^2 is characterized by a significantly larger amount of MW energy transferred to the particle internal energies. The particle temperature in case 3 decreases to 2300 K in the first half of the nozzle, due to fast gas–particle energy transfer and then increases to over 2600 K in the second half of the nozzle. The particle surface temperature quickly decreases in the plume where the MW energy is not deposited.

The gas temperature fields for the three cases under consideration, shown in Fig. 9b, illustrate strong coupling between the particle internal energies and the gas translational energies. In the first two cases, the gas translational temperature is only slightly smaller than the corresponding particle surface temperatures. For case 3, the difference between gas and particle temperatures is larger and amounts to about 300 K at the nozzle exit plane. Even though a significant amount of radiation has been deposited into alumina particles, their temperature is still lower than the particle boiling temperature of 3250 K.

The impact of the MW beam/alumina particle coupling on gas velocities in the axial direction is shown in Fig. 10a. As expected, the presence of MW radiation has a smaller effect on gas velocities than on gas and particle temperatures. The gas velocity at the nozzle exit increases for case 2 by less than 0.5%, as compared to the no-radiation case. For case 3 it increases by approximately 2% in both the core flow and near the nozzle lip. The MW energy deposition has a minor effect on gas densities, as illustrated in Fig. 10b. It slightly improves flow directionality in case 3, in which a smaller difference between the gas density in the core flow and near the nozzle surface is observed. Near the nozzle axis, the gas density at the nozzle exit plane is about 3% higher for case 3. Near the nozzle lip, it is up to 25% lower. The computed thrust increases from 1.77 MN for case 1 to 1.78 MN for case 2 to 1.88 MN for case 3. The pressure increase in the diverging part of the nozzle for the 1 GW/m^2 is approximately a factor of 2 of the unaugmented case, well within the factor of safety for a Castor 120 nozzle.

In addition to the computational modeling of a Castor 120 nozzle expansion, numerical analysis has been conducted for an Orion 50S XL type of nozzle. A conical geometry was chosen for the diverging part of the nozzle, with an expansion ratio of 34.3 and an exit diameter of 0.712 m, which correspond to the actual nozzle geometry. Similar to the Castor 120 case, the simulations were conducted from the nozzle throat to the near field of the nozzle, with uniform boundary conditions set at the throat. The throat temperature, density, and velocity were 2500 K, 2.49 kg/m^3, and 1326 m/s, respectively. A single effective gas species and a single alumina particle size of 4 μm were used with an alumina particle loading of 32%. The results obtained for this nozzle are both qualitatively and quantitatively similar to those for Castor 120. MW energy deposition (again, 0.1 and 1 GW/m^2 intensities were used) results in noticeable increase in gas temperature, as shown in

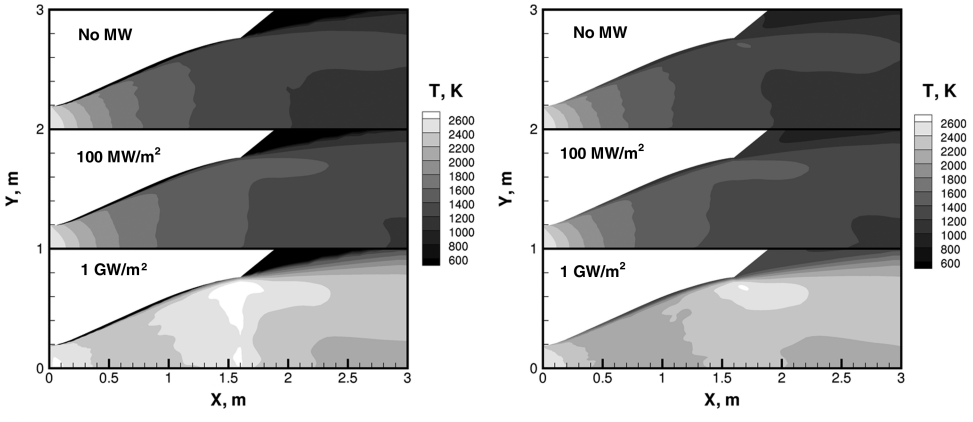

Fig. 9 Castor 120 temperatures (K) for the different MW intensities: a) particle and b) gas.

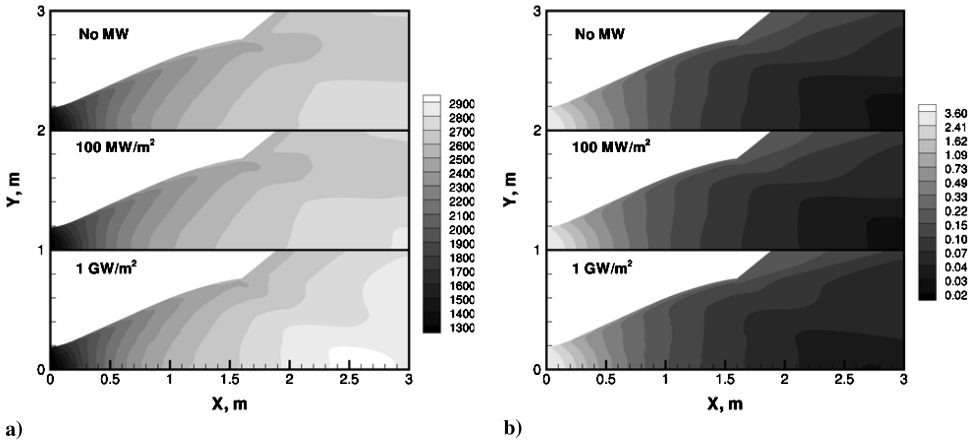

Fig. 10 Castor 120 for different MW intensities: a) gas axial velocity (m/s) and b) gas density (kg/m^3).

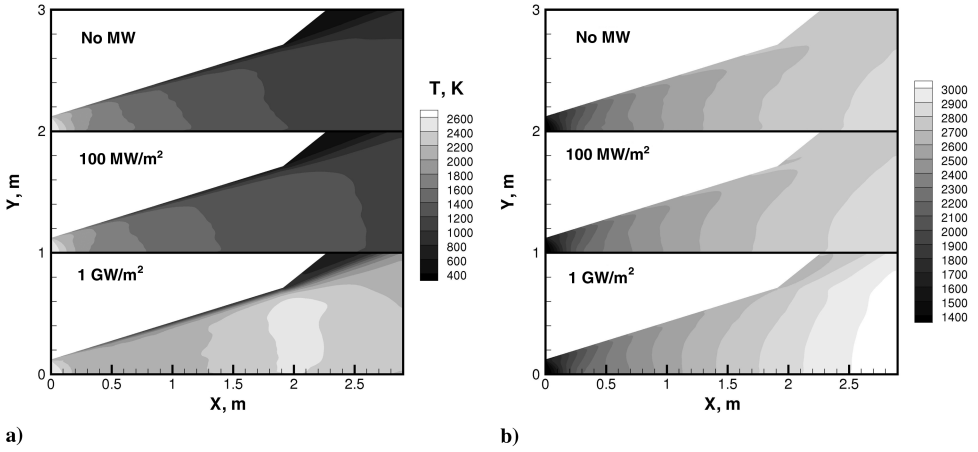

Fig. 11 Orion 50S for different MW intensities: a) gas temperature (K) and b) gas velocity (m/s).

Fig. 11a. For a 1 GW/m^2 MW intensity, the gas temperature in the core flow at the nozzle exit plane increase from about 1200 to over 2400 K. The change in the exit velocities is much smaller, though increasing from 2720 to about 2850 m/s at the centerline. The changes in both temperature and velocity are small for a 0.1 GW/m^2 intensity, resulting in relatively modest increases in thrust, due to MW energy deposition. The thrust increased from 0.623 MN for the no-MW case to 0.626 MN for 0.1 GW/m^2 case and 0.663 MN for 1 GW/m^2 case.

VIII. Conclusions

The feasibility of using a high-intensity MW beam to increase the thrust of a solid rocket motor over the first part of a typical launch trajectory has been studied, through the deposition of the radiation energy into the internal energy of alumina particles in the diverging part of the nozzle. The analysis shows that for high-enough intensities of the MW beam (larger than 1 GW/m^2), the following assumptions may generally be made:

1) The alumina particles are quickly heated to their boiling temperature near the nozzle throat and then kept at that temperature as they move to the nozzle exit.

2) The gas–particle heat transfer is very fast and so the gas comes to thermal equilibrium with particles over distances much smaller than the length of the diverging part of the nozzle.

The second assumption seems reasonable for Castor 120 and Orion 50S XL types of motors, based on the numerical results presented earlier. However, the first assumption requires very large MW intensities to be applied. With the above assumptions, the expansion of the gas in the diverging part of the nozzle is affected by a heat source (alumina particles) that keeps the gas near the boiling temperature of alumina.

Experimental results indicate that a coupling efficiency of MW energy to alumina particles could be relatively large (e.g., of upwards of 57% at a particle temperature of 816 K) for this system. The power-generation system presented in this study consists of an array of 665 total parabolic antennas, drawing 3.13 GW of input power in order to produce a nominal 1.0 GW at the launch vehicle at an altitude of 50 km. A CFD analysis was conducted to investigate the performance characteristics associated with energy coupling to a solid rocket motor plume. A Castor 120 motor was considered as an example of a high-thrust launch motor, and 2 MW intensities have been considered: 100 MW/m^2 and 1 GW/m^2. In the high-density environment of a Castor 120 type of motor, MW energy was found to be transferred effectively to the internal energy of alumina particles. The absorbed MW energy in the particles is subsequently transferred to the surrounding gas kinetic energy, increasing the total thrust. An Orion 50S XL motor was also analyzed. Both motors showed very similar results with the total thrust increasing about 6% for the 1 GW/m^2 case. The total jet power also increased about 10% for both motors in the 1 GW/m^2 case.

Acknowledgments

The authors wish to acknowledge the support of the Advanced Concepts Group of the U.S. Air Force Research Laboratory's Propulsion Directorate, Edwards Air Force Base, California. The support of Marcus Young was particularly helpful. The assistance of Sean Hammerland is also greatly appreciated.

References

[1] Tsiolkovsky, K., *Spaceship, 1924, in Izbrannye Trudy, Izdatel'stvo Akademii Nauk, SSSR*, 1962, p. 222 (in Russian).

[2] Shad, J. L., and Moriarty, J. J., "Microwave Rocket Concept," *XVI International Astronautical Congress*, Athens, 1965, pp. 175–186.

[3] Parkin, K. G., "The Microwave Thermal Thruster and Its Application to the Launch Problem," Ph.D. Dissertation, California Inst. of Technology, Pasadena, CA, 2006.

[4] Parkin, K. G., Di Domenico, L. D., and Culick, F., "The Microwave Thermal Thruster Concept," *Proceedings of the Second International Symposium: Beamed Energy Propulsion*, edited by K. Komurasaki, AIP Conference Proceedings, American Inst. of Physics, Melville, NY, 2004, pp. 418–429.

[5] Parkin, K. G., and Culick, F., "Feasibility and Performance of the Microwave Thermal Rocket Launcher," *Proceedings of the Second International Symposium: Beamed Energy Propulsion*, edited by K. Komurasaki, AIP Conference Proceedings, Vol. 702, American Inst. of Physics, Melville, NY, 2004, pp. 407–417.

[6] Oda, Y., Komurasaki, K., Takahashi, K., Kasugai, A., and Sakamoto, K., "Plasma Generation Using High-Power Millimeter-Wave Beam and Its Application for Thrust Generation," *Journal of Applied Physics*, Vol. 100, 2006, Paper 113307. doi:10.1063/1.2399899

[7] Nakagawa, T., Yorichika, M., Komurasaki, K., Takahashi, K., Sakamoto, K., and Tsuyoski, I., "Propulsive Impulse Measurement of a Microwave-Boosted Vehicle in the Atmosphere," *Journal of Spacecraft and Rockets*, Vol. 41, No. 1, 2004, pp. 151–153. doi:10.2514/1.2540

[8] Hilden, J., and Poirier, B., "Castor 120^{TM} Motor: Development and Qualification Testing Results," AIAA Space Programs and Technologies Conference and Exhibits, AIAA Paper 93-4277, Huntsville, AL, Sept. 1993.

[9] *Pegasus User's Guide*, Release 6.0, Orbital Sciences Corp., Dulles, VA, Jan. 2007.

[10] Benford, J., and Dickinson, R., "Space Propulsion and Power Beaming Using Millimeter Systems," *Intense Microwave Pulses III*, Proceedings of SPIE: The International Society for Optical Engineering, Vol. 2557, SPIE, Bellingham, WA, 1995.

[11] Benford, J., and Swegle, J., *High Power Microwaves*, 2nd ed., Series in Plasma Physics, Taylor and Francis, New York, 2007.

[12] Jory, H., Blank, M., Borchard, P., Cahalan, P., Cauffman, S., Chu, T., and Felch, K., "CPI Gyrotrons for Fusion EC Heating," *High Energy Density and High Power RF: 7th Workshop on High Energy Density and High Power RF*, edited by D. Abe and G. Nusinovich, AIP Conference Proceedings, American Inst. of Physics, Melville, NY, pp. 180–190.

[13] Brown, W. C., "The Technology and Application of Free-Space Power Transmission by Microwave Beam," *Proceedings of the IEEE*, Vol. 62, No. 1, 1974, pp. 11–25. doi:10.1109/PROC.1974.9380

[14] Cornella, B., Hammerland, S., Ketsdever, A., and Song, H., "Power Generation for a Beamed Microwave Propulsion Concept," 45th AIAA/ASME/SAE/ASEE Joint Propulsion Conference and Exhibit, AIAA Paper 2009-4872, Denver, CO, Aug. 2009.

[15] Simmons, F. S., *Rocket Exhaust Plume Phenomenology*, Aerospace Press, El Segundo, CA, 2000.

[16] Sutton, W. H., "Microwave Processing of Ceramic Materials," *Ceramic Bulletin*, Vol. 68, No. 2, 1989, pp. 376–386.

[17] Bykov, Y., Rybakov, K., and Semenov, V., "High-Temperature Microwave Processing of Materials," *Journal of Physics D: Applied Physics*, Vol. 34, 2001, pp. R55–R75. doi:10.1088/0022-3727/34/13/201

[18] Fukushima, H., Yamanaka, T., and Matsui, M., "Microwave Heating of Ceramics and Its Application to Joining," *Journal of Materials Research*, Vol. 5, No. 2, 1990, pp. 397–405. doi:10.1557/JMR.1990.0397

[19] Toth, G., "General Code for Modeling MHD flows on Parallel Computers: Versatile Advection Code," *Astrophysical Letters and Communications*, Vol. 34, 1997, pp. 245–250.

[20] Chakravarthy, S., and Peroomian, O., "Some Internal Flow Applications of a Unified-Grid CFD Methodology," 32nd AIAA/ASME/SAE/ASEE Joint Propulsion Conference and Exhibit, AIAA Paper 96-2926, Lake Buena Vista, FL, July 1996.

[21] Gimelshein, S., Markelov, G., and Muylaert, J., "Numerical Modeling of Low Thrust Solid Propellant Nozzles at High Altitudes," 37th AIAA Plasmadynamics and Lasers Conference, AIAA Paper 2006-3273, San Francisco, June 2006.

[22] Mingos, D. M. P., "Theoretical Aspects of Microwave Dielectric Heating," *Microwave Assisted Organic Synthesis*, edited by J. P. Thierney and P. Lindstrom, Blackwell Science, Boston, 2000, pp. 1–21.

[23] Braginsky, V. B., Ilchenko, V. S., and Bagdassarov, K. S., "Experimental Observation of Fundamental Microwave Absorption in High-Quality Dielectric Crystals," *Physics Letters A*, Vol. 120, No. 6, 1987, pp. 300–306. doi:10.1016/0375-9601(87)90676-1

[24] Fukushima, H., Yamanaka, T., and Matsui, M., "Measurement of Dielectric Properties of Ceramics at Microwave Frequency," *Journal of the Japan Society for Precision Engineering*, Vol. 53, 1987, pp. 743–748.

E. Kim
Associate Editor